



Deposited via The University of Leeds.

White Rose Research Online URL for this paper:

<https://eprints.whiterose.ac.uk/id/eprint/171690/>

Version: Accepted Version

Article:

Šindija, D, Neuberg, J and Smith, P (2021) The complex, static displacement of a very long period seismic signal observed at Soufrière Hills volcano, Montserrat, WI. *Journal of Volcanology and Geothermal Research*, 413. 107209. ISSN: 0377-0273

<https://doi.org/10.1016/j.jvolgeores.2021.107209>

© 2021, Elsevier. This manuscript version is made available under the CC-BY-NC-ND 4.0 license <http://creativecommons.org/licenses/by-nc-nd/4.0/>.

Reuse

This article is distributed under the terms of the Creative Commons Attribution-NonCommercial-NoDerivs (CC BY-NC-ND) licence. This licence only allows you to download this work and share it with others as long as you credit the authors, but you can't change the article in any way or use it commercially. More information and the full terms of the licence here: <https://creativecommons.org/licenses/>

Takedown

If you consider content in White Rose Research Online to be in breach of UK law, please notify us by emailing eprints@whiterose.ac.uk including the URL of the record and the reason for the withdrawal request.

1 **The complex, static displacement of a very long**
2 **period seismic signal observed at Soufrière Hills**
3 **volcano, Montserrat, WI**

4 **Dinko Šindija^{a,*}, Jürgen Neuberg^a, Patrick Smith^{b,c}**

5 ^a*School of Earth and Environment, University of Leeds, Leeds, LS2 9JT, UK*

6 ^bMontserrat Volcano Observatory, Flemmings, Montserrat, West Indies

7 ^cNow at: Dublin Institute for Advanced Studies, 5 Merrion Square, Dublin 2, Ireland

8 **Abstract**

In this study we demonstrate how very-long period (VLP) volcanic seismic signals can be processed in order to obtain essential and detailed information about the seismo-volcanic source process. As an example we use the VLP signal observed on 23 March 2012 during an outgassing event at Soufrière Hills volcano, Montserrat, acquired by instruments with different natural periods. The aim of this study is to highlight the importance of retrieving the correct source time function by a complete restitution process. When ground displacement cannot be retrieved through the restitution process due to very narrow band-pass limited instrument response, we compare synthetic and observed waveforms in the velocity domain and determine the best model by generating a synthetic velocity seismogram using the band-limited seismometer characteristics. Furthermore, we show how this approach of forward modelling can reveal much more detail of the source process, since small changes in displacement are enhanced in the velocity seismogram. Using these restituted and modelled displacements we perform a moment tensor inversion combined with a grid search locating the source at 600 m depth below sea level and estimating the source volume change to be in the range of

$0.6 - 1.1 \times 10^3 \text{ m}^3$.

9 **1. Introduction**

10 Volcanogenic seismic signals cover a broad frequency range and fall into three
11 main categories, and their interpretation and modelling are at the core of any
12 attempt to forecast volcanic eruptions. Volcano-tectonic (VT) earthquakes, gen-
13 erated by the brittle failure of the rocks around the fault plane due to the stress
14 changes of magmatic emplacement or due to pressure changes as a result of water-
15 magma interaction in hydrothermal systems (Neuberg, 2020) have the same char-
16 acteristics as tectonic earthquakes: clear P- and S-wave onsets and frequency con-
17 tent of 1-20 Hz. Low-frequency (LF) earthquakes have successfully been used in
18 forecasting volcanic eruptions (e.g. Chouet, 1996). They have a spectral range
19 between 0.2 and 10 Hz, with end members of the continuum being Long-Period
20 (LP) events and hybrid events, which are similar to LP events but have additional
21 high frequency onset (Neuberg, 2020). Their source processes differ significantly
22 from the ones for generation of VTs. LF earthquakes originate at the boundary
23 between magmatic fluid and solid surrounding rock (e.g. Chouet, 1988; Neuberg
24 et al., 2000) or can be caused by slow, quasi-brittle low stress-drop failure driven
25 by short-lived upper-edifice deformation (Bean et al., 2014). The deployment and
26 widespread use of broadband seismic networks in the 1990s made studies of very-
27 long period (VLP) signals possible (Kawakatsu et al., 1992; Neuberg et al., 1994)
28 and we focus in our study on this category. VLP signals, whose periods range from
29 several seconds to several minutes, have been observed on almost every type of vol-
30 cano around the world (Chouet and Matoza, 2013). When the periods of these

31 signals fall into the far end of the range they are often referred to as an ultra-long
32 period (ULP) seismic signals. The event we are describing in this study falls into
33 that range of ULPs, however we choose to call it a VLP as the source process
34 between these two types of signals does not differ. Their source processes are usu-
35 ally attributed to fluid-rock interactions such as mass movement of volcanic fluids
36 (e.g. Chouet and Dawson, 2011) generating abrupt pressure changes inside the
37 volcanic edifice. As VLPs have been observed prior to caldera collapse (Kumagai
38 et al., 2001; Michon et al., 2009) and prior to phreatic eruptions (Kawakatsu et al.,
39 2000; Jolly et al., 2017) the need to study them is of great importance for under-
40 standing the underlying physical processes. Therefore, it is essential to retrieve the
41 exact source time history in addition to amplitude and moment tensor compon-
42 ents. The major advantage VLP signals offer is direct insight in the deformation
43 of the source process. This fact was recognised and studied by Legrand et al.
44 (2000, 2005). In this study we emphasise the importance of taking into account
45 how different seismometers influence the observed signals and what the necessary
46 processing steps are in order to retrieve the maximum amount of information from
47 the observed waveforms. These processing steps go beyond the usual “instrument
48 removal” applied as a routine by seismic processing packages, which considers the
49 frequency range in the pass-band of the instrument only. In contrast, we try to
50 retrieve information cut-out by the instrument and subsequently, use this inform-
51 ation in our moment tensor inversion to estimate the location and mechanism of
52 the source. As an example we use a VLP signal observed on 23 March 2012 during
53 a outgassing event at Soufrière Hills volcano (SHV), Montserrat.

54 **2. Data acquisition**

55 At the time of the event the seismic network on the island of Montserrat con-
56 sisted of nine stations equipped with three-component broadband seismometers.
57 Due to recording problems, the number of stations available for this study was
58 reduced to six: Waterworks (MBWW) station, deployed by the University of
59 Leeds, equipped with a 120s Güralp-3T broadband instrument, Broderick’s Yard
60 (MBBY) and Windy Hill (MBWH) stations with 60s Güralp-3ESPC broadband
61 instruments, and stations Fergus Ridge (MBFR), St. George’s Hill (MBGH),
62 and Roche’s Yard (MBRY) equipped with 30s Güralp-40T broadband instruments
63 (Figure 1). All data were recorded with a sampling rate of 100 Hz and were
processed using the software package Obspy (Krischer et al., 2015).

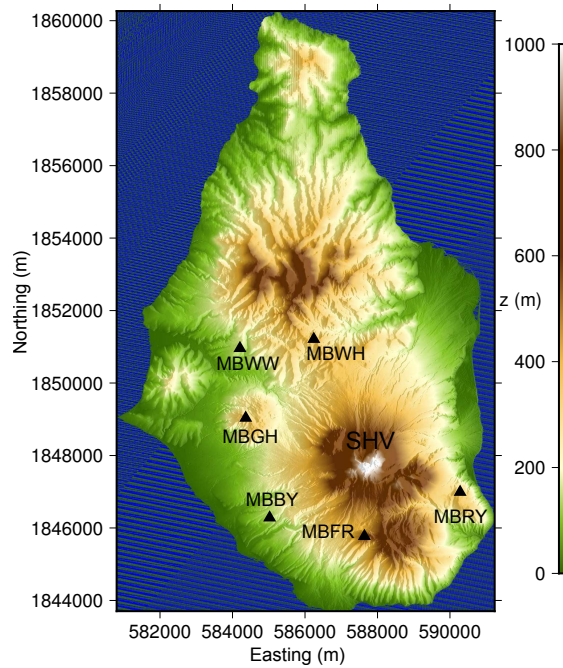


Figure 1: Topographic map of Montserrat with 6 operational stations on March 23, 2012

64

65 **3. Seismicity on 23 March 2012**

66 The eruption of SHV began in 1995 and has consisted of five phases of magma
67 extrusion, the last of which ended on 11 February 2010. After more than two years
68 of quiescence with no lava extrusion and low seismicity, two swarms of around 50
69 volcano-tectonic (VT) earthquakes occurred at SHV on 22 and 23 March 2012
70 (Smith, 2015). The most intense VT swarm lasted for around 15 minutes, starting
71 at 07:10 UTC on 23 March 2012. During this swarm, a local magnitude (M_L) 3.9
72 VT earthquake was observed at 07:20 UTC making it the largest VT earthquake
73 ever observed on Montserrat till that date (Cole et al., 2012). This was followed by
74 three hybrid events that terminated the swarm at 07:22 UTC (Cole et al., 2012).
75 A VLP signal was observed across the MVO (Montserrat Volcano Observatory)
76 seismic network during this swarm coinciding with a large amplitude strain signal
77 (~ 280 nano strain) recorded on borehole strainmeters on the island (Hautmann
78 et al., 2014). Several hours after this swarm, a short episode of ash venting began
79 and an elevated SO_2 flux was recorded between 23 and 27 March - peaking at
80 4600 t/day on 26 March 2012.

81 **4. Data Processing**

82 *4.1. VLP signal identification*

83 Although some VLP seismicity can be seen clearly on broadband velocity seis-
84 mograms (e.g. Jolly et al., 2017), VLP signals often cannot easily be identified
85 in the velocity domain. This is due to the instrument acting as a differentiator
86 converting ground displacement to velocity, i.e. the instrument amplifies the high
87 frequencies. Furthermore, a band-pass filter is applied defined by the instrument
88 response. Often, the first step in searching for a VLP signal is analysing the amp-

89 litude spectrum of the velocity trace. In our example we see a broad peak relating
 90 to the VLP signal around 0.01 Hz (Figure 2a). However, this VLP signal has been
 91 distorted by the instrument response as the low frequencies in the original signal
 92 have been cut-off. Hence, when analysing VLP signals that have a frequency con-
 93 tent outside the flat-band of the instrument response, one needs to keep in mind
 94 the original signal could contain seismic energy at much longer periods than dis-
 95 played in the amplitude spectrum of the recorded signal. Figure 2b shows such an
 96 example where a signal with dominant period of 500s is observed at the station
 97 with the 120 second instrument.

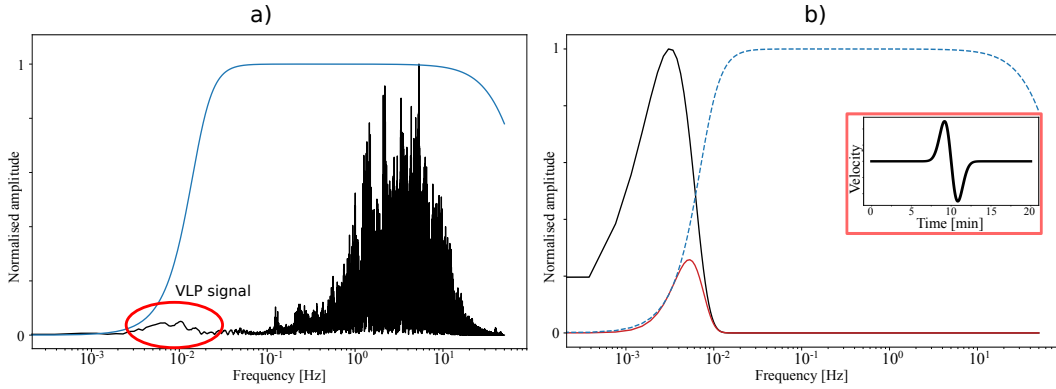


Figure 2: a) Amplitude spectrum of the vertical component velocity seismogram recorded at MBWW station on March 23, 2012 showing a broad VLP signal with dominant frequency of 0.01 Hz with superimposed transfer function of 120s-instrument at that station. b) Example of how the instrument response impacts the observed amplitude spectrum. We produced a synthetic velocity seismogram with period of 500 seconds (red box), calculated the amplitude spectrum (black) and then simulated the effect of the 120s-instrument response on the input signal (red).

98 Another simple way to identify a VLP signal when it is not directly observable
 99 on the velocity seismogram is to integrate the velocity seismogram or apply a low-
 100 pass filter. Figure 3a shows a 16 minute long record of the VT swarm observed on
 101 23 March 2012. The velocity seismogram is dominated by the high frequency VT
 102 earthquakes. However, if we integrate the seismogram (Figure 3b) the VLP signal

103 becomes obvious. In this case we see two clear VLP signals, one starting at 07:16
104 UTC and the other one, with much larger amplitude, at 07:19 UTC. In this study
105 we focus on the second, larger amplitude signal.

106 *4.2. Restitution of the ground displacement*

107 To account for the shape of the instrument response and to make sure that
108 the restitution of ground displacement considers the whole energy content of the
109 ground motion we have to carry out certain processing steps. The process of resti-
110 tution of the ground displacement is depicted in Figure 3. We apply different
111 high-pass filters with cut-off frequencies of 0.004 Hz, 0.002 Hz, and 0.001 Hz to
112 the velocity trace after which we remove the instrument response (including the
113 digitiser gain) and integrate the trace to obtain the displacement seismogram (Fig-
114 ure 3 c-e). The application of a high-pass filter with a cut-off frequency lower than
115 the flat-band of the instrument response (Neuberg and Lockett, 1996; Caudron
116 et al., 2018) helps us recover the low frequency information while suppressing the
117 amplification of the long period, environmental and electronic noise during the
118 integration. Choosing the appropriate high pass filter is crucial, as the interpret-
119 ation of the obtained displacement seismograms changes. Trace (c) shows with
120 an apparent inflation (motion up) followed by a deflation (motion down) below
121 the original level. This interpretation dramatically changes by including longer
122 periods in traces (d) and (e). The ground displacement shown now in trace (e)
123 could be described as a step-like inflation. The fact that a further extension to
124 a lower frequency range does not change the waveform indicates that the trace
125 now represents the “true” ground displacement of the process. In this case it gives
126 us the “true” amplitude of the displacement as well, which can be directly read
127 from the displacement seismogram (Figure 3f). Unfortunately there is no general

128 recipe or criteria how to define the lowest cut-off frequency as this process highly
 129 depends on the data quality. In general, the vertical components are less affected
 130 by low frequency noise than the horizontal components. We also have to assume
 131 that there is no seismic energy or a static offset at even lower frequencies.

132 The restitution process comprises the application of the inverse instrument
 133 transfer function using complex Poles and Zeros (PAZ) response files provided by
 134 the manufacturer. The integration from velocity to displacement can be carried
 135 separately or by including an extra term $(s - 0)$ in the inverse instrument transfer
 136 function (Scherbaum, 2001)

$$137 \quad \mathcal{U}_g = c' \frac{(s - p_1)(s - p_2)(s - p_3) \cdots (s - p_{np})}{(s - z_1)(s - z_2)(s - z_3) \cdots (s - z_{nz})(s - 0)} \mathcal{X}_{\text{vel}}, \quad (1)$$

138 where \mathcal{U}_g is the displacement seismogram, \mathcal{X}_{vel} the recorded velocity seismogram,
 139 nz is number of zeros z and np is number of poles p , while c' is the overall norm-
 140 alisation constant containing also the digitiser gain.

141 4.3. Forward modelling of ground displacement

142 Due to the very low frequency content in our example, this restitution method
 143 was not applicable for the stations equipped with instruments with natural periods
 144 shorter than 120 s. These instruments have a much lower signal to noise ratio at
 145 long periods. A way around this problem is using the following forward modelling
 146 technique: we assume a ground displacement model, or adopt the one determined
 147 by the 120s instrument as a starting model. Next we apply the instrument response
 148 of 60s or 30s seismometers to this trace and compare the resulting synthetic velo-
 149 city seismogram with the velocity data. This is done similarly to the restitution
 150 process, however when we apply the instrument response (i.e. multiplying the
 151 displacement model with the transfer function, hence simulating the recording

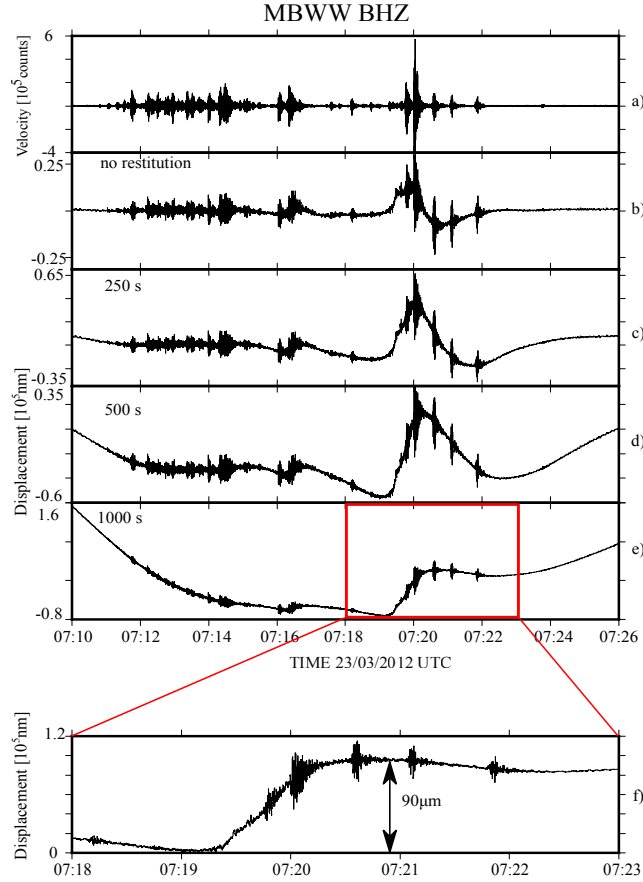


Figure 3: Restitution of the vertical component ground displacement at MBWW station. (a) Uncorrected velocity seismogram. (b) Integrated (without restitution) velocity seismogram which identifies the VLP signal (c) to (e) Displacement seismograms after correcting for the instrument response and considering spectral components to a period of 250, 500 and 1000 s respectively. (f) Five minute long time window showing true ground displacement.

152 process), an extra Zero in our PAZ response files equals differentiation when we
 153 move from the displacement to the velocity domain. As a starting model for ground
 154 displacement we use an approximation of the waveform that we obtained from the
 155 vertical component of the 120 s instrument at the MBWW station. Vertical com-
 156 ponents are generally less affected by the noise than the horizontal components.
 157 One has to be aware that such an approach makes all following results highly de-

158 pendent on the single station MBWW. If the instrument response is even slightly
159 incorrect the effect will be carried across the network into all synthetic displace-
160 ment seismograms and, therefore, into the model. Similarly, any other noise at
161 MBWW would be carried through to the rest of the stations.

162 In the limited 5 min time window shown in Figure 3f, the restituted signal
163 appears to be a step function, however, outside this time window the long term
164 behaviour cannot be uniquely determined. As the signal was recorded with a velo-
165 city sensor (seismometer) a static offset represented by the step function will always
166 decay to zero. Nevertheless, focusing on the source process in our volcanological
167 study, we are interested in the initial slope of the signal. Therefore, in contrast to
168 VLP signals on other volcanoes that are observed and interpreted as oscillatory
169 behaviour (e.g. Dawson and Chouet, 2014; Caudron et al., 2018), we assume the
170 model of a step-like displacement. We model it by using the Richards Growth
171 Equation (RGE), a generalised logistic function defined by upper (K) and lower
172 (A) asymptotes, the curve growth rate (B), the time of the maximum growth (M),
173 and the asymmetry parameter (ν) (Richards, 1959; Green and Neuberg, 2005):

$$174 \quad Y(t) = A + \frac{K - A}{[1 + e^{B(t-M)}]^{1/\nu}}. \quad (2)$$

175 We adjust the parameters of the step function to match the restituted ground
176 displacement of the vertical component of the 120s instrument (Figure 4). This
177 trace is now used as input to create the synthetic velocity seismograms for the
178 120s, 60s, and 30s instruments, respectively. First we apply the 120s instrument
179 response (including differentiation), apply a low-pass filter and compare it with
180 the low-passed data of MBWW (Figure 4). The comparison shows that even
181 though the amplitude of the step function is well constrained by the restituted

182 data from the MBWW station, the modelled step function does not match the
183 detailed time history in the velocity domain. The same discrepancy is also seen
184 when comparing the resulting velocity seismograms of the band-limited stations
185 with the original data on other components and stations. Upon more detailed
186 analysis of the restituted ground displacement at MBWW we noticed a change of
187 slope in the step function approximately 1.5 minutes (t_0) into the trace. To model
188 this discontinuity, we designed a two-phase step function using the RGE as a basis
189 to see if a change in the slope can explain the discrepancy in the velocity domain.
190 The modified step function is therefore divided into two phases, Y_{phase1} and Y_{phase2}
191 (Figure 4) described respectively as:

$$192 \quad Y_{\text{phase1}}(t) = A_1 + \frac{K_1 - A_1}{[1 + e^{B_1(t-M_1)}]^{1/\nu_1}}, \quad t \leq t_0 \quad (3)$$

$$193 \quad Y_{\text{phase2}}(t) = A_2 + \frac{K_2 - A_2}{[1 + e^{B_2(t-M_2)}]^{1/\nu_2}}, \quad t > t_0. \quad (4)$$

195 A crucial assumption we make is that the change in the slope happens at the
196 same time for all components at all stations. Due to the wavelength of the signal,
197 the arrival time difference at different station is negligible, therefore we can take
198 this assumption into an account. The function is made continuous by selecting A_2
199 which minimises $|\max(Y_{\text{phase1}}) - \min(Y_{\text{phase2}})|$. Applying the instrument response
200 to this model for ground displacement produces a synthetic velocity seismogram
201 which better matches the data in the velocity domain. Now that we have shown
202 this model works for a station equipped with 120s instrument, we examine how
203 well our ground displacement model fits at stations equipped with 60 s and 30 s
204 instruments. While for station MBWW the displacement model is fitted to the
205 restituted ground displacement, for other stations we use the simulated annealing

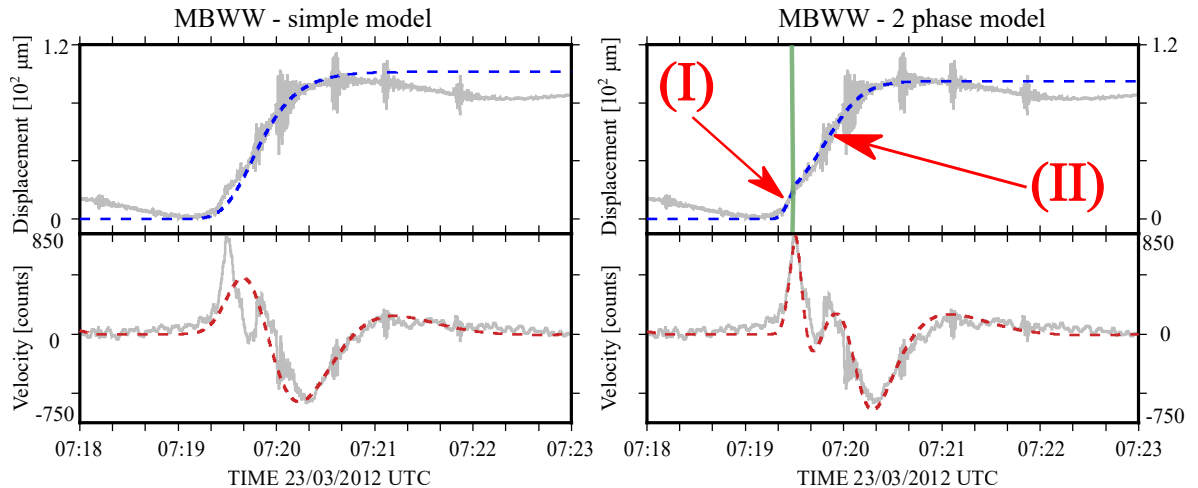


Figure 4: Ground displacement models (blue dashed lines) based on the restituted ground displacement (grey) at MBWW on March 23, 2012; using a simple step function (left) and using a 2 phase step function (right). We apply the band-pass limited instrument response and differentiate both ground displacement models and then compare the resulting synthetic velocity data (red dashed line) with the low passed filtered (below 20s) observed data (grey). The green vertical line represents the onset time of the change of slope and the roman numerals represent the two phases of our modeled step function.

206 (SA) method (Du and Swamy, 2016) to determine the best fit. We vary the
 207 ground displacement model parameters and the goodness of a fit is measured in
 208 the velocity domain. A 95 % confidence interval has been included in the overall
 209 step amplitude estimate. Therefore, a 10% uncertainty in the estimate of the step
 210 amplitude linearly translates into 10 % uncertainty in the volume change estimate
 211 in Section 5.2. Using the method of Wielandt and Forbriger (1999) we also removed
 212 the effect of the tilt from the horizontal components. Our results show that the two-

213 step model can explain the observed velocity waveforms on all available stations in
214 the network for both the vertical and horizontal components (Figure 5, Appendix
215 A). Furthermore, the results from 60 and 30 s stations reinforce our selection of
216 the 1000 s high-pass filter as an appropriate one for the restitution process because
217 if our ground displacement were not a step-like function it would not provide the
218 very good match in the velocity domain. While the combined fit in velocity and
219 displacement domain was necessary to circumvent the band-width limitations of 30
220 and 60s instruments, this approach also revealed the advantages capturing details
221 in the time history of the signal in the velocity domain.

222 **5. Source mechanism and location**

223 *5.1. Method*

224 Only after we perform the appropriate restitution process, obtaining the amp-
225 litude and time history of the observed displacements, can we evaluate the volume
226 change at the source by performing a moment tensor inversion (MTI) using the
227 software package VOLPIS (Cesca and Dahm, 2008). By using this method we can
228 resolve both the moment tensor (MT) and single force (SF) components as well as
229 the source time history. As we are mostly interested in the combined amplitude
230 of the two-phase source displacement, we model the static displacement again as
231 a simple step function (Equation 2). These are modelled individually for each
232 component at each station based on the two-phase step function so the start, end,
233 and the maximum amplitude of the static displacement is equal. Additionally, as
234 VOLPIS is a frequency domain inversion code, the large static step at the end of
235 our displacement models makes the inversion unstable. Therefore we differentiate

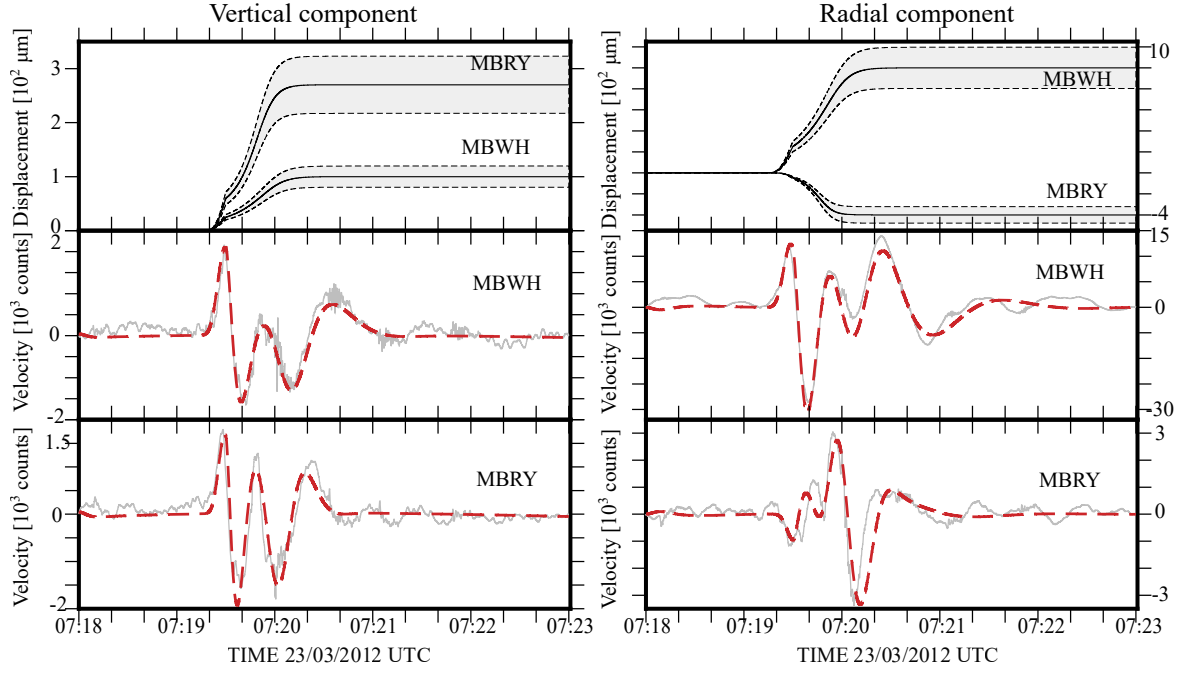


Figure 5: Vertical (left) and radial (right) component of the modelled ground displacements for stations MBWH and MBRY using the 2 phase step functions. The 95 % confidence intervals are shown as grey shaded areas. After simulating the instrument response we compare the synthetic velocity data (red dashed line) with the observed data (grey). Low-pass filter with cut-off frequency of 20s is applied to both synthetic and observed data.

236 the resulting displacement step models:

$$237 \quad v(t) = \frac{d}{dt}Y(t) = \mathcal{F}^{-1} [j\omega\mathcal{Y}(\omega)], \quad \mathcal{Y}(\omega) = \mathcal{F} [Y(t)] \quad (5)$$

238 where $v(t)$ represents the velocity trace, $Y(t)$ is a simple step function, and the \mathcal{F}
 239 indicates the Fourier transform. The MTI is therefore performed in the velocity
 240 domain resulting in the moment rate components. The resolved moment rate
 241 components are then integrated and can be directly compared with the source
 242 time history used for modelled displacements. The Green's functions are computed

243 using a spectral element method SPECFEM3D (Komatitsch et al., 2012), for a
 244 volumetric grid ($2.0\text{km} \times 1.2\text{km} \times 0.8\text{km}$) (Figure 6) of possible source locations
 245 with grid spacing of 200 m centred below the summit of SHV. The topography
 246 is included in the calculation of the Green’s functions assuming a homogeneous
 247 halfspace with $v_p = 3500$ m/s, $v_s = 2000$ m/s, and $\rho = 2600$ kg/m³. As the
 248 VLP signals have wavelengths much larger than the source-receiver distances, we
 249 do not expect any influence from subsurface heterogeneities, and the assumption
 250 of a homogeneous halfspace is justified. We perform the MTI for each point in
 251 the grid and estimate the location of the source by finding the minimum misfit
 252 between observed displacement seismograms and obtained synthetic displacement
 253 seismograms through our inversion using:

$$\text{misfit} = \left[\frac{\sum_{i=1}^{N_t} \sum_{j=1}^{M_i} (d_i(t_j) - s_i(t_j))^2}{\sum_{i=1}^{N_t} \sum_{j=1}^{M_i} (d_i(t_j))^2} \right], \quad (6)$$

255 where N_t is the number of time traces, M_i is the number of time samples for
 256 j -th trace, and $d_i(t_j)$ and $s_i(t_j)$ are the j -th samples of i -th time trace for input
 257 data and synthetic time trace respectively (Cesca and Dahm, 2008). The misfit
 258 results are dimensionless and normalised. The data were downsampled to 3 Hz
 259 and bandpassed between 0.001 and 1 Hz. The inversions are done whilst keeping
 260 the constraint for the source parameters to have same time histories for the MT
 261 and SF components.

262 5.2. Results

263 The best-fitting model was located to be at depth of 600 m, 1000 m east and
 264 400 m south of the volcano summit (Figure 6). The resulting waveform fit (Figure

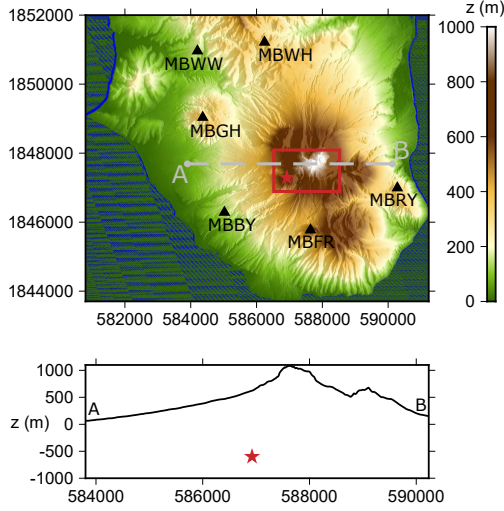


Figure 6: (top) Zoomed in map of Montserrat showing the horizontal boundaries of the volumetric grid of possible source locations (red triangle). Location of the best-fitting model is shown with the red star. (bottom) Cross section profile (extracted from point A to point B) showing the depth of the source and its relative location from the summit of the SHV.

265 7) shows a fairly good fit for all three components at all stations. The resulting
 266 moment and single force rate time histories are shown in Figures 8. By normalising
 267 the resolved moment tensor (Figure 8):

$$268 \quad \mathbf{M} = M_0 \begin{bmatrix} M_{nn} & M_{ne} & M_{nz} \\ M_{en} & M_{ee} & M_{ez} \\ M_{zn} & M_{ze} & M_{zz} \end{bmatrix} = 3.8 \times 10^{13} \begin{bmatrix} 0.53 & -0.29 & -0.55 \\ -0.29 & 0.13 & -0.44 \\ -0.55 & -0.44 & 0.73 \end{bmatrix} \text{ Nm} \quad (7)$$

269 we estimate the scalar seismic moment to be 3.8×10^{13} Nm. The resolved vector
 270 of single forces is:

$$271 \quad \mathbf{F} = F_0 \begin{bmatrix} F_n \\ F_e \\ F_z \end{bmatrix} = 3.3 \times 10^{10} \begin{bmatrix} 0.17 \\ -0.75 \\ -0.64 \end{bmatrix} \text{ N} \quad (8)$$

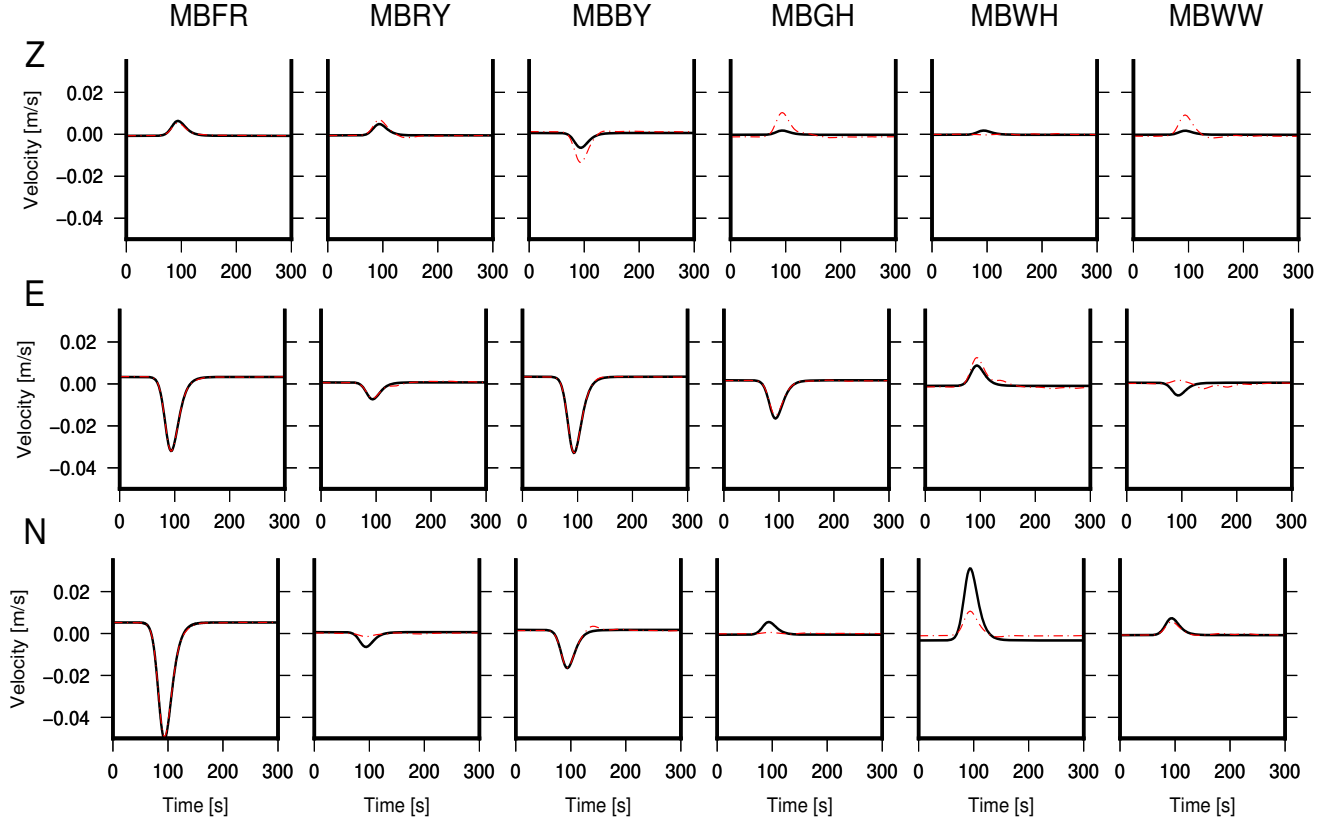


Figure 7: The seismogram fit in the velocity for three components at the available stations for the March 2012 event. Black solid line represents our input data for the inversion, while the dashed red line represents the best-fit solution synthetic data.

272 Comparing the maximum amplitudes of single force components (8) and their mo-
273 ment counterparts we see that $|\frac{SF_{\text{north}}}{M_{xx}}| = 0.0003 \text{ m}^{-1}$, $|\frac{SF_{\text{east}}}{M_{yy}}| = 0.005 \text{ m}^{-1}$, and
274 $|\frac{SF_{\text{vert}}}{M_{zz}}| = 0.0007 \text{ m}^{-1}$ demonstrating that the single force components are negli-
275 gible. We follow the decomposition of the resolved moment tensor by Vavryčuk
276 (2001) and calculate the percentage of isotropic component to be 64%, CLVD
277 component 12%, and double couple component to be 24%. The shear component
278 has a strike of 187° , dip 21° , and rake 146° . The volume change (ΔV) at the
279 source is then estimated using $\Delta V = \frac{M_{\text{iso}}}{(\lambda + \frac{2}{3}\mu)}$, where M_{iso} represent isotropic

280 moment and λ and μ are Lamé parameters. Assuming a Poisson's ratio $\nu = \frac{1}{4}$
 281 ($\lambda = \mu$) and our model space velocities, we estimate the source volume change to
 282 be $\Delta V = (1015 \pm 100) \text{ m}^3$. However, for volcanic rocks at or near liquidus temper-
 283 ature it may be more appropriate to use a Poisson's ratio $\nu = \frac{1}{3}$ ($\lambda = 2\mu$) (Murase
 284 and McBirney, 1973) which results in a source volume change $\Delta V = (635 \pm 60) \text{ m}^3$.

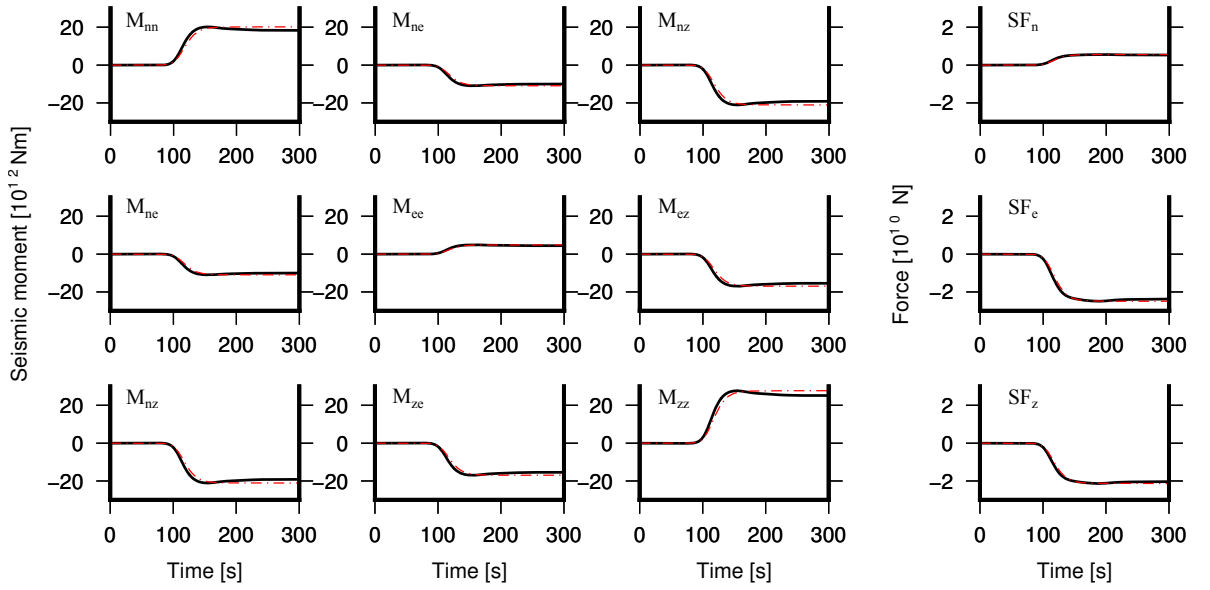


Figure 8: The resolved source time histories for the moment tensor and single force components (black). We multiply the average source time function used for the modelled displacements with the moment tensor/ single force component (dashed red line) so we can compare how well the shape of the displacement step function is resolved.

285 6. Discussion

286 This event demonstrates the need to include in the restitution of ground dis-
 287 placement the spectral components of the VLP signal that go beyond the nat-
 288 ural period of the seismometer. When ground displacements cannot be retrieved
 289 through a restitution process, we show how by modelling ground displacements and
 290 accounting for the seismometer response, we can compare synthetic and observed

291 waveforms in the velocity domain and determine the best model. Additionally, we
292 show in our example how forward modelling can reveal more details of the source
293 process, since small changes in displacement are enhanced in the velocity domain.
294 As VLP signals have wavelengths of 10s to 100s of km, it places all of our seismic
295 stations in the so-called near-field, i.e. within one wavelength from the source. In
296 the near-field, the seismic displacement at the surface is directly proportional to
297 the deformation at the source. In our example, where we observe a signal with a
298 dominant period of approximately 100 s, equivalent to a wavelength of 350 km,
299 all stations are in the near field and we can relate our restituted displacement and
300 models to a source volume change. The two-phase step function describing the dis-
301 placement at the source, has not been seen in such detail before. The result implies
302 that the source volume change happened in two-phases, a rapid onset and then a
303 slower continuation of the motion. We cannot say whether this type of motion is
304 due to the source itself acting in two phases or whether the slower continuation
305 of the motion is due to a rebound effect of the surrounding medium, however this
306 question lies outside the scope of this study. This process differs from a previous
307 VLP observed on SHV Green and Neuberg (2005) which had larger observed dis-
308 placements but a simpler source time history. Unlike the signal analysed by Green
309 and Neuberg (2005) where only vertical component seismograms at two stations
310 were used, this event was observed on all three components at six stations in the
311 seismic network. Although the azimuthal coverage of the network was not perfect,
312 the observations still show that the same source time history can be seen on all
313 components. It also allows us to perform moment tensor inversion to improve our
314 interpretation of the source mechanics, although it is necessary to consider the ef-
315 fect of the network coverage in the estimation of the source mechanism and source

316 volume change. If the inversions do not converge to a unique solution, we still
317 could have a good fit in the displacement/velocity domain, however the resolved
318 MT/SF components could not be resolved. We can directly relate the observations
319 at the surface to the source mechanism, by comparing the inverted time histories
320 of moment tensor and single force components with the modelled source time func-
321 tion and, hence, obtain another verification of our moment tensor inversion result.
322 Those show the source mechanism of the best-fitting model is an explosion with a
323 strong shear component (Figures 8). The source volume change for the best fitting
324 model is estimated to be in the range of $0.6 - 1.1 \times 10^3 \text{ m}^3$. Using strain data from
325 3 borehole dilatometers, Hautmann et al. (2014) described this ash venting event
326 as being initiated by the ascent of magmatic fluid from deeper magmatic system
327 into shallow dyke. However, based on our estimate of volume change and depth
328 we can speculate that it is not the sudden movement of magma that initiated this
329 event, but rather it was due to CO_2 flushing. If an amount of free gas phase of
330 CO_2 , degassing at larger depths, hits a supersaturated magma batch it can get
331 the water out of the solution and cause a sudden volume change (Caricchi et al.,
332 2018). Looking at a broader aspect of the previous eruptive behaviour of SHV,
333 such modulations could have been a trigger for the onset of a new eruptive phase
334 which would explain why it is not the overpressure or a certain volume recharge
335 that needs to be reached to start an eruptive phase (Figure 9).

336

337 7. Conclusions

338 The analysis of the VLP signal observed on 23 March 2012 during an outgassing
339 and ash-venting event on Soufrière Hills Volcano, Montserrat provides a great ex-

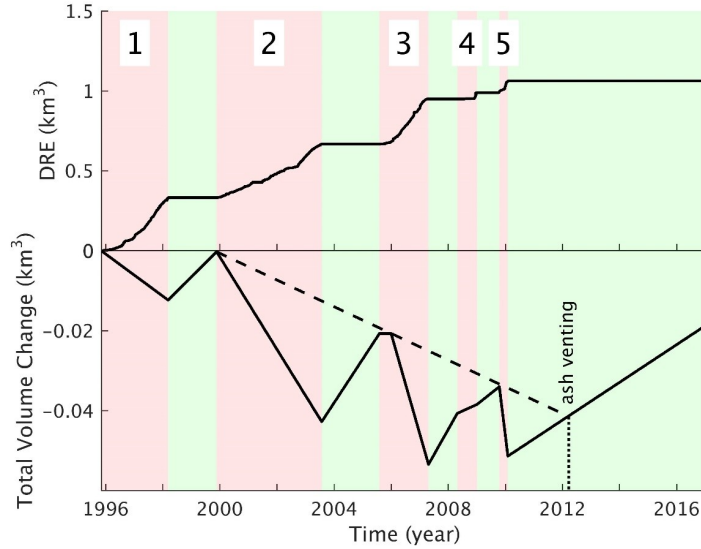


Figure 9: Approximation of the cumulative source volume change since the start of the eruption in 1995. The volume extruded during eruptive phase always exceeds the volume replenished during quiet periods. The dashed line marks the onset of renewed extrusions and links it to the timing of the ash-venting episode studied here. Adapted from Neuberg et al. (2018)

340 ample how the VLP signals can and should be processed. It is of great importance
 341 to carry out the proper processing steps in order to retrieve the maximum amount
 342 of information from the observed seismograms if we want to interpret source mech-
 343 anism of VLP signals correctly. We show how forward modelling of the ground
 344 displacement can reveal much more details of the source process, since the small
 345 changes in displacement are enhanced in the velocity seismogram. Additionally
 346 we perform moment tensor inversions and estimate the source mechanism to be
 347 an isotropic mechanism with a strong shear component. The resulting volume
 348 change, potentially caused by CO₂ flushing is estimated to be in the range of
 349 $0.6 - 1.1 \times 10^3 \text{ m}^3$. By combining the results from our restitution process, forward
 350 modelling, and the moment tensor inversion we interpret the source mechanism
 351 of the event to be an volume opening with a complex, static source displacement

352 with a strong shear component acting in a two-phase motion with a rapid onset
353 and a slower continuation of the motion.

354 **Acknowledgments**

355 D. Šindija is funded by the University of Leeds Research Scholarship. J.
356 Neuberg is partly funded by the Centre for the Observation and Modelling of
357 Earthquakes, Volcanoes and Tectonics (COMET NE/J01978X/1). The seismic
358 data is curated by Montserrat Volcano Observatory and can be made available
359 upon request to mvo@mvo.ms. This work was undertaken on ARC3, part of the
360 High Performance Computing facilities at the University of Leeds, UK. We thank
361 the two anonymous reviewers for their insightful comments that improved the
362 original manuscript.

363 **References**

- 364 Bean, C.J., De Barros, L., Lokmer, I., Métaxian, J.P., O'Brien, G., Murphy, S.,
365 2014. Long-period seismicity in the shallow volcanic edifice formed from slow-
366 rupture earthquakes. *Nature Geoscience* 7, 71–75.
- 367 Caricchi, L., Sheldrake, T.E., Blundy, J., 2018. Modulation of magmatic processes
368 by CO_2 flushing. *Earth and Planetary Science Letters* 491, 160–171.
- 369 Caudron, C., Taisne, B., Neuberg, J., Jolly, A.D., Christenson, B., Lecocq, T.,
370 Suparjan, Syahbana, D., Suantika, G., 2018. Anatomy of phreatic eruptions.
371 *Earth, Planets and Space* 70, 168.
- 372 Cesca, S., Dahm, T., 2008. A frequency domain inversion code to retrieve time-
373 dependent parameters of very long period volcanic sources. *Computers &*
374 *Geosciences* 34, 235–246.

375 Chouet, B., 1988. Resonance of a fluid-driven crack: Radiation properties and
376 implications for the source of long-period events and harmonic tremor. *Journal*
377 *of Geophysical Research: Solid Earth* 93, 4375–4400.

378 Chouet, B., Dawson, P., 2011. Shallow conduit system at Kilauea Volcano, Hawaii,
379 revealed by seismic signals associated with degassing bursts. *Journal of Geo-*
380 *physical Research: Solid Earth* 116.

381 Chouet, B., Matoza, R., 2013. A multi-decadal view of seismic methods for de-
382 tecting precursors of magma movement and eruption. *Journal of Volcanology*
383 *and Geothermal Research* 252, 108 – 175.

384 Chouet, B.A., 1996. Long-period volcano seismicity: its source and use in eruption
385 forecasting. *Nature* 380, 309–316.

386 Cole, P., Bass, V., Christopher, T., Odbert, H., Smith, P., R., S., Stinton, A.,
387 Syers, R., Williams, P., 2012. MVO scientific report for volcanic activity between
388 1 November 2011 and 30 April 2012.

389 Dawson, P., Chouet, B., 2014. Characterization of very-long-period seismicity ac-
390 companying summit activity at Ka’lauea Volcano, Hawai’i: 2007-2013. *Journal*
391 *of Volcanology and Geothermal Research* 278-279, 59.

392 Du, K.L., Swamy, M.N.S., 2016. *Simulated Annealing*. Springer International
393 Publishing, Cham. pp. 29–36.

394 Green, D.N., Neuberg, J., 2005. Seismic and infrasonic signals associated with an
395 unusual collapse event at the Soufrière Hills volcano, Montserrat. *Geophysical*
396 *Research Letters* 32, L07308.

397 Hautmann, S., Witham, F., Christopher, T., Cole, P., Linde, A.T., Sacks, I.S.,
398 Sparks, R.S.J., 2014. Strain field analysis on Montserrat (W.I.) as tool for
399 assessing permeable flow paths in the magmatic system of Soufrière Hills volcano.
400 *Geochemistry, Geophysics, Geosystems* 15, 676–690.

401 Jolly, A., Lokmer, I., Thun, J., Salichon, J., Fry, B., Chardot, L., 2017. In-
402 sights into fluid transport mechanisms at White Island from analysis of coupled
403 very long-period (VLP), long-period (LP) and high-frequency (HF) earthquakes.
404 *Journal of Volcanology and Geothermal Research* .

405 Kawakatsu, H., Kaneshima, S., Matsubayashi, H., Ohminato, T., Sudo, Y., Tsut-
406 sui, T., Uhira, K., Yamasato, H., Ito, H., Legrand, D., 2000. Aso94: Aso
407 seismic observation with broadband instruments. *Journal of Volcanology and*
408 *Geothermal Research* 101, 129–154.

409 Kawakatsu, H., Ohminato, T., Ito, H., Kuwahara, Y., Kato, T., Tsuruga, K.,
410 Honda, S., Yomogida, K., 1992. Broadband seismic observation at the Sakur-
411 ajima volcano, Japan. *Geophysical Research Letters* 19, 1959–1962.

412 Komatitsch, D., Vilotte, J.P., Tromp, J., Ampuero, J.P., Bai, K., Basini, P., Blitz,
413 C., Bozdog, E., Casarotti, E., Charles, J., Chen, M., Galvez, P., Goddeke, D.,
414 Hjorleifsdottir, V., Labarta, J., Le Goff, N., Le Loher, P., Lefebvre, M., Liu,
415 Q., Luo, Y., Maggi, A., Magnoni, F., Martin, R., Matzen, R., McRitchie, D.,
416 Meschede, M., Messmer, P., Michea, D., Nadh Somala, S., Nissen-Meyer, T.,
417 Peter, D., Rietmann, M., de Andrade, E., Savage, B., Schuberth, B., Sieminski,
418 A., Strand, L., Tape, C., Xie, Z., Zhu, H., 2012. *Specfem3d cartesian v2.0.2*
419 [software]. doi:<http://doi.org/NoDOI>.

- 420 Krischer, L., Megies, T., Barsch, R., Beyreuther, M., Lecocq, T., Caudron, C.,
421 Wassermann, J., 2015. Obspy: a bridge for seismology into the scientific Python
422 ecosystem. *Computational Science and Discovery* 8, 014003.
- 423 Kumagai, H., Ohminato, T., Nakano, M., Ooi, M., Kubo, A., Inoue, H., Oikawa, J.,
424 2001. Very-long-period seismic signals and caldera formation at Miyake Island,
425 Japan. *Science* 293, 687–690.
- 426 Legrand, D., Kaneshima, S., Kawakatsu, H., 2000. Moment tensor analysis of
427 near-field broadband waveforms observed at Aso Volcano, Japan. *Journal of*
428 *volcanology and geothermal research* 101, 155–169.
- 429 Legrand, D., Rouland, D., Frogneux, M., Carniel, R., Charley, D., Roullet, G.,
430 Robin, C., 2005. Interpretation of very long period tremors at Ambrym volcano,
431 Vanuatu, as quasi-static displacement field related to two distinct magmatic
432 sources. *Geophysical research letters* 32.
- 433 Michon, L., Villeneuve, N., Catry, T., Merle, O., 2009. How summit calderas col-
434 lapse on basaltic volcanoes: New insights from the april 2007 caldera collapse of
435 Piton de la Fournaise volcano. *Journal of Volcanology and Geothermal Research*
436 184, 138–151.
- 437 Murase, T., McBirney, A.R., 1973. Properties of some common igneous rocks and
438 their melts at high temperatures. *Geological Society of America Bulletin* 84,
439 3563–3592.
- 440 Neuberg, J., Barclay, J., Burton, M., Calder, E., Fournier, N., Rivalta, E., 2018.
441 Assessment of the hazards and risks associated with the Soufrière Hills Volcano,

442 Montserrat. 22nd Report of the Scientific Advisory Committee on Montserrat
443 Volcanic Activity (Full Report) .

444 Neuberg, J., Lockett, R., 1996. Seismo-volcanic sources on Stromboli volcano .

445 Neuberg, J., Lockett, R., Baptie, B., Olsen, K., 2000. Models of tremor and
446 low-frequency earthquake swarms on Montserrat. *Journal of Volcanology and*
447 *Geothermal Research* 101, 83 – 104.

448 Neuberg, J., Lockett, R., Ripepe, M., Braun, T., 1994. Highlights from a seismic
449 broadband array on Stromboli volcano. *Geophysical Research Letters* 21, 749–
450 752.

451 Neuberg, J.W., 2020. *Earthquakes, Volcanogenic*. Springer International Publish-
452 ing, Cham. pp. 1–10.

453 Richards, F.J., 1959. A flexible growth function for empirical use. *Journal of*
454 *Experimental Botany* 10, 290–300.

455 Scherbaum, F., 2001. *Of poles and zeros: fundamentals of digital seismology.*
456 volume 15. 2nd ed., Kluwer Academic, Dordrecht;London;.

457 Smith, P., 2015. Volcano-tectonic seismicity of Soufriere Hills volcano, Montserrat.
458 *Encyclopedia of Earthquake Engineering* , 3907–3919.

459 Vavryčuk, V., 2001. Inversion for parameters of tensile earthquakes.
460 *Journal of Geophysical Research: Solid Earth* 106, 16339–16355. URL:
461 <http://dx.doi.org/10.1029/2001JB000372>, doi:10.1029/2001JB000372.

462 Wielandt, E., Forbriger, T., 1999. Near-field seismic displacement and tilt associ-
463 ated with the explosive activity of Stromboli. *Annals of Geophysics* 42.

464 Appendices

465 Appendix A

466 Here we show the residual seismogram from the Wielandt and Forbriger (1999)
467 method for tilt removal. Figure 10 shows the removal of the tilt component at
468 station MBWW. After the tilt is removed from the horizontal components we
469 rotate the seismograms back to north and east seismograms. The effect of the tilt
470 signal is shown in Figure 11 for the north component at MBWW.

471 Appendix B

472 Figures 12 and 13 show the displacement models for all three components and at
473 all stations. We apply the seismometer response to these models and then compare
474 it with the band-passed velocity seismograms. Both the synthetic and original
475 velocity seismograms are filtered between 20 and 1000 seconds. The horizontal
476 components are rotated into radial and transverse components, then we remove
477 the influence of tilt signals, after which the resulting traces are rotated back into
478 east and north components. The backazimuth is derived from the particle motion
479 using the horizontal components.

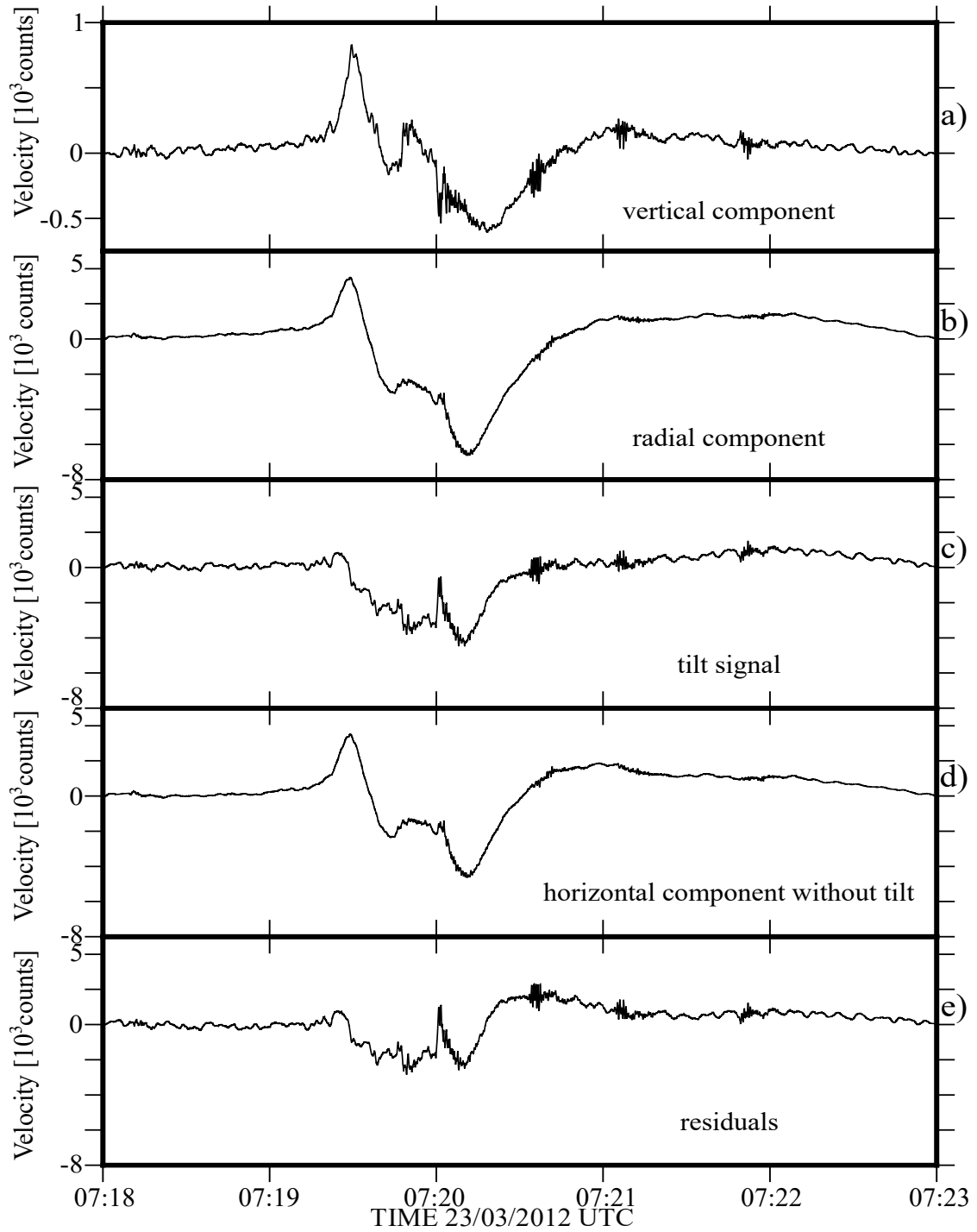


Figure 10: Trace a) is the vertical component velocity trace band-passed between 1000 and 20s. Traces c) and d) show the radial component after removal of the displacement and tilt component respectively, and e) shows the residual after removing both components from the horizontal trace.

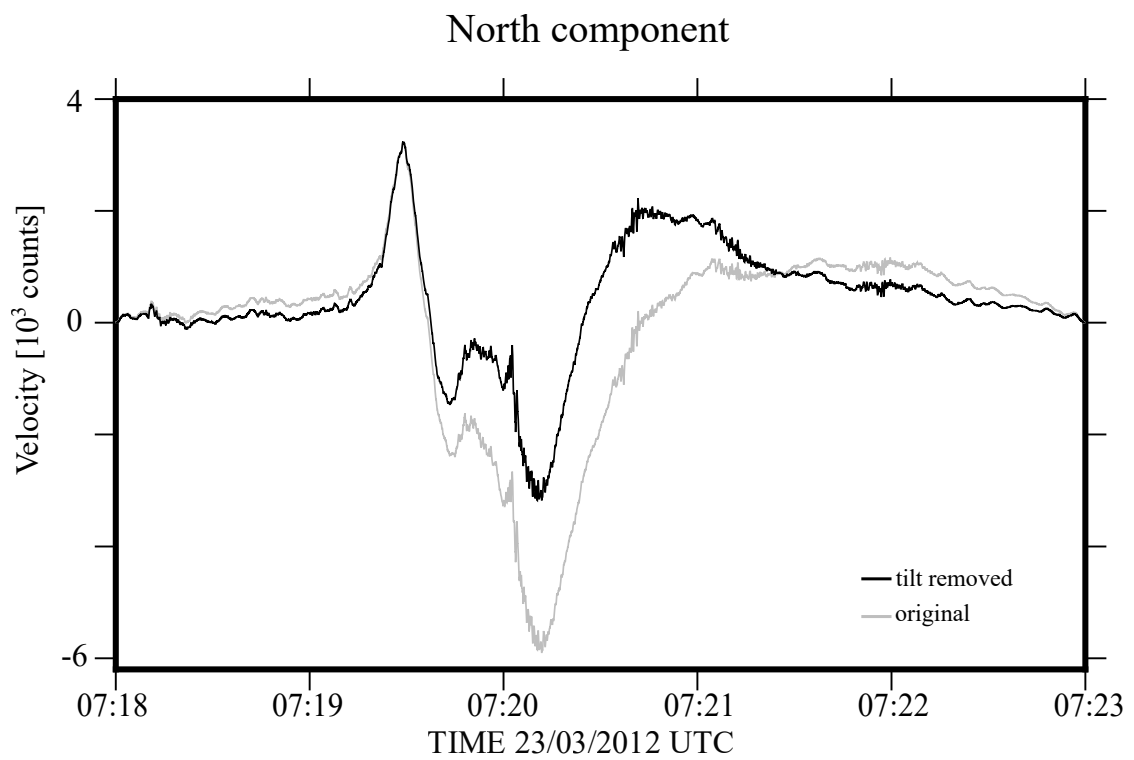


Figure 11: North component velocity seismogram at MBWW station before (grey) and after (black) removal of the tilt.

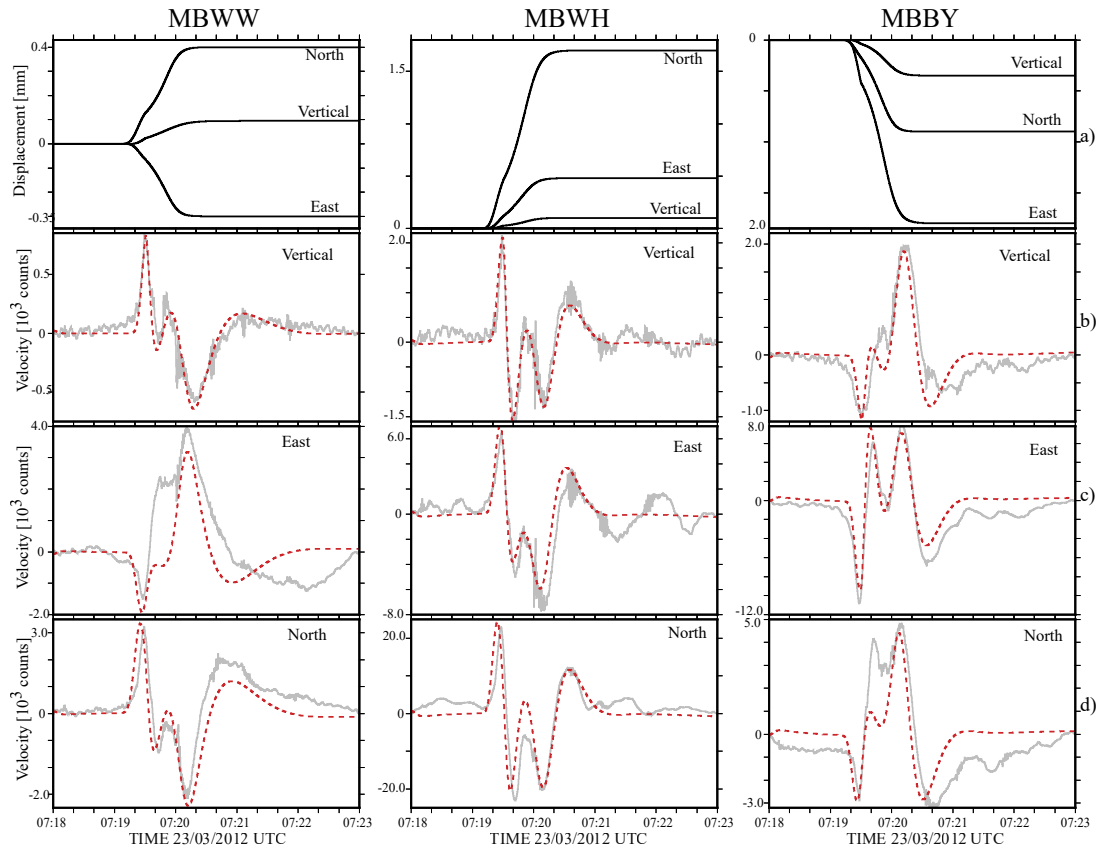


Figure 12: (a) Displacement models for all three components at stations MBWW, MBWH, and MBBY. (b-d) After applying the instrument response and differentiating the resulting synthetic velocity seismogram is band-passed (red dotted) and compared with the band-passed velocity seismogram (grey). The velocity seismograms are filtered between 0.001 and 0.05 Hz.

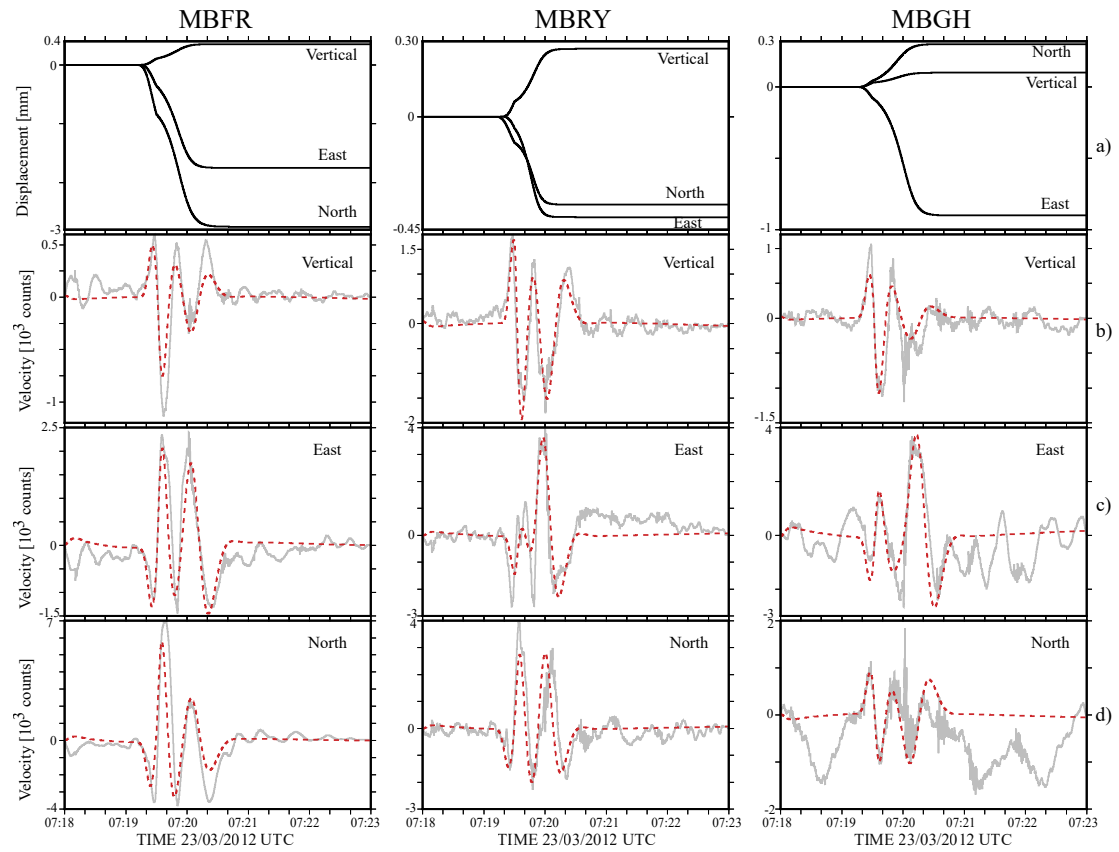


Figure 13: (a) Displacement models for all three components at stations MBFR, MBRY, and MBGH. (b-d) After applying the instrument response and differentiating the resulting synthetic velocity seismogram is band-passed (red dotted) and compared with the band-passed velocity seismogram (grey). The velocity seismograms are filtered between 0.001 and 0.05 Hz.